




# Residual thickness enhanced core-removed D-shaped single-mode fiber and its application for VOC evaporation monitoring

HUADAN ZHENG,<sup>1,2,3,5</sup> BINCHENG HUANG,<sup>3,5</sup> YUHAN LI,<sup>3</sup> RENJING ZHANG,<sup>3</sup> XIAOHANG GU,<sup>1</sup> ZHINBIN LI,<sup>1</sup> HAORYANG LIN,<sup>1</sup> WENGUO ZHU,<sup>1,6</sup>  JIEYUAN TANG,<sup>1</sup> HEYUAN GUAN,<sup>1,3</sup> HUIHUI LU,<sup>1,3</sup> YONGCHUN ZHONG,<sup>1,3</sup> JUNBIN FANG,<sup>1,3</sup> YUNHAN LUO,<sup>1</sup> JUN ZHANG,<sup>1,3</sup> JIANHUI YU,<sup>1,3,7</sup> FRANK K TITTEL,<sup>4</sup> AND ZHE CHEN<sup>1,3</sup>

<sup>1</sup>Key Laboratory of Optoelectronic Information and Sensing Technologies of Guangdong Higher Education Institutes, Department of Optoelectronic Engineering, Jinan University, Guangzhou, 510632, China

<sup>2</sup>State Key Laboratory of Applied Optics, Changchun Institute of Optics, Fine Mechanics and Physics, Chinese Academy of Sciences, Changchun 130033, China

<sup>3</sup>Guangdong Provincial Engineering Technology Research Center on Visible Light Communication and the Guangzhou Municipal Key Laboratory of Engineering Technology on Visible Light Communication, Jinan University, Guangzhou, 510632, China

<sup>4</sup>Department of Electrical and Computer Engineering, Rice University, Houston, Texas 77005, USA

<sup>5</sup>These authors contributed equally to the manuscript

<sup>6</sup>zhuwg88@163.com

<sup>7</sup>kensomyu@gmail.com

**Abstract:** A core-removed D-shaped structure with different residual thickness (RT) was manufactured on a single mode silica fiber (SMF) to enhance the sensitivity by using of ultra-precise polishing technology. With six different RTs ranging from  $\sim 55\ \mu\text{m}$  to  $\sim 28\ \mu\text{m}$ , the RT enhancement effect in a D-shaped SMF was researched in detail. The influence of the RT on its transmission spectra was investigated both theoretically and experimentally. Considering a compromise between the multimode interference efficiency and optical power loss, an optimum RT value of  $34.09\ \mu\text{m}$  was achieved. The obtained refractive index (RI) sensitivity was  $10243\ \text{nm/RIU}$  in the RI range of  $1.430\text{--}1.444$ , corresponding to a RI resolution of  $1.9 \times 10^{-6}\ \text{RIU}$ . A high-performance all-fiber sensor was developed to monitor the evaporation process volatile organic compounds (VOCs) based on the RT-enhanced D-shaped SMF. As proof of concept, a 2-hour continuous monitoring was carried to monitor the chloroform and alcohol mixture. As a result, the evaporation of alcohol and chloroform were clearly identified and monitored. The developed RT-enhanced D-shaped fiber sensor provides an alternative way for chemical process monitoring and industrial applications.

© 2020 Optical Society of America under the terms of the [OSA Open Access Publishing Agreement](#)

## 1. Introduction

The refractive index (RI) sensor based on an optical fiber with the advantages of no electromagnetic interference, compact structure and high sensitivity has been widely researched in the past [1]. Of the optical fiber sensors, multimode interference (MMI) is an effective approach to improve the detection sensitivity, which was investigated in the past years [2]. Multimode interference in optical waveguide refers to light of each conduction mode which interferes with each other. This causes an optical field distribution in the cross section of the fiber which changes periodically along the longitudinal transmission distance. The surrounding refractive index (SRI) affects the multimode interference effect in the optical waveguide and transmission spectra. The MMI plays an important role in various fields such as fiber sensors [3–10], couplers [11–13], optical

filters [14,15] and fiber lasers [16]. For MMI-based fiber RI sensors, efficient excitation of high-order modes and a strong evanescent field in the multimode waveguide section is desirable, since the RI changes are related to the MMI spectra shift. Various kinds of fiber sensors such as coreless fiber [17,18], tapered fiber [6] and small core fiber [19] were reported. Among them, the side-polished fiber (SPF) [20] was a fiber made by polishing a section of the fiber cladding with optical micro-machining technology. To fabricate the SPF, the part of cladding of single-mode fiber (SMF) was side-polished to make the remaining cladding as a D-shaped multimode waveguide. The cladding thickness of the fiber was polished to an area of only a few microns in the core. The light transmitted in the core will leak out in the form of an evanescent wave field, providing a strong interaction with external media. The SPF based on MMI was sensitive to surrounding refractive index. Based on this principle, the material to be tested was positioned in the side-polished area and the evanescent wave field was able to interact with the material. The SPF provides a wonderful platform for refractive index sensing. According to the MMI principle and the D-shaped structure, several RI sensors based on MMI were reported, such as the side-polished single mode-multimode-single mode fiber [21], a multi-D-Shaped optical fiber [22], and side-polished plastic optical fiber [23]. However, most of the D-shaped fibers are based on multi-mode fibers or plastic fibers with large cores.

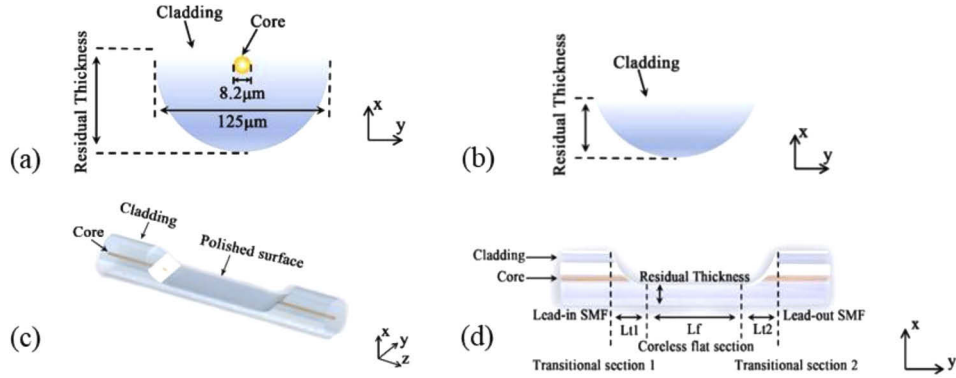
In this paper, a core-moved D-shaped structure was fabricated on a single mode silica fiber by a custom ultra-precise polishing system. The whole core of the SMF was removed to obtain high multimode interference. Six different RTs from 55  $\mu\text{m}$  to 28  $\mu\text{m}$  was researched to optimize the RT-enhancement in detail. The transmission spectra through the RT-enhanced D-shaped SMF were investigated both theoretically and experimentally. With an optimized RT of 35  $\mu\text{m}$ , a RT-enhanced D-shaped fiber sensor was developed for VOCs mixture evaporation monitoring. The VOC monitoring principle and performance was analyzed in detail.

## 2. Principle

### 2.1. Structure of RT-enhanced D-shaped SMF

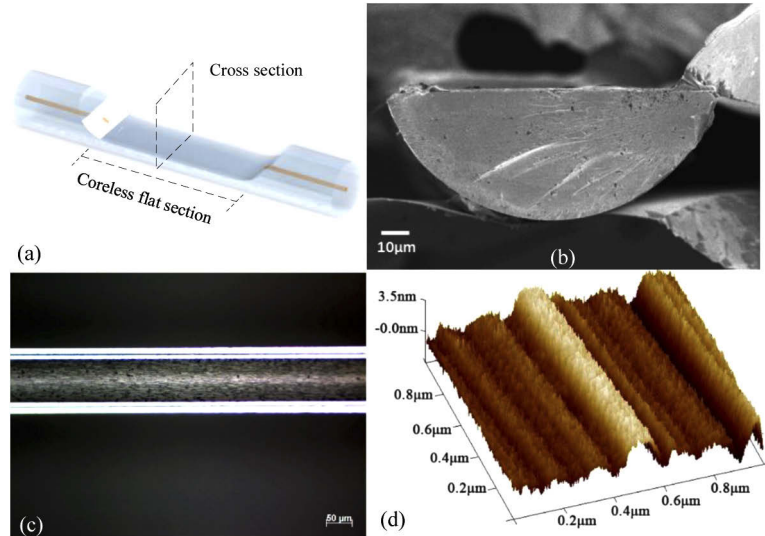
The basis of a fiber-optic index sensor is the interaction between the analyte and evanescent wave fields in the fiber. In order to get access to evanescent wave fields it is necessary to remove portions of the fiber cladding. The removal can be performed by fiber fusing and a tapering technique, a fiber side polishing technique and femtosecond laser pulses. Fibers with cladding removed on one side are referred to as side-polished fibers (SPF), as shown in Fig. 1(a). The vertical dimension from the polished surface to the fiber surface, which is referred to as the residual thickness (RT) in Fig. 1(a), is an important parameter which determines the strength of the interaction of the evanescent wave fields with external media. In our previous publications, various fiber sensors based on SPF were reported such as fiber couplers [24], modulators [25], attenuators [26], switcher [27], humidity sensors [28,29] and a temperature sensor [30]. However, the previous publications report only the partial removal of the fiber cladding. This work reports the removal of the whole fiber core as shown in Fig. 1(b), which is referred to as the RT-enhanced D-shaped SMF. Figure 1(c) shows the three-dimensional structure of a RT-enhanced D-shaped SMF. Both the cladding and core were polished by the precisely controlled fiber fabrication system. Five minutes of rough polishing was carried out to fabricate the SPF. An additional finishing polishing procedure was carried out to fabricate the RT-enhanced D-shaped SMF. The fiber fabrication can be done within 10 mins using our custom polishing system. Figure 1(d) depicts the side view of the RT-enhanced D-shaped SMF. The RT-enhanced D-shaped SMF can be divided into five sections: lead-in SMF, transitional section 1, coreless flat section, transitional section 2 and a lead-out SMF. As described by the simulations in the next manuscript section, the coreless flat section worked as a D-shaped multimode waveguide. The curve polished surface of the transitional section 1 provided an efficient way to excite the high-order modes by multi reflection and scattering. The strong evanescent field on the fiber polishing surface provide a high

sensitivity sensing area for the surrounding refractive index. The fiber core in the transitional section 2 collects the light from the coreless flat section for the output measurements.



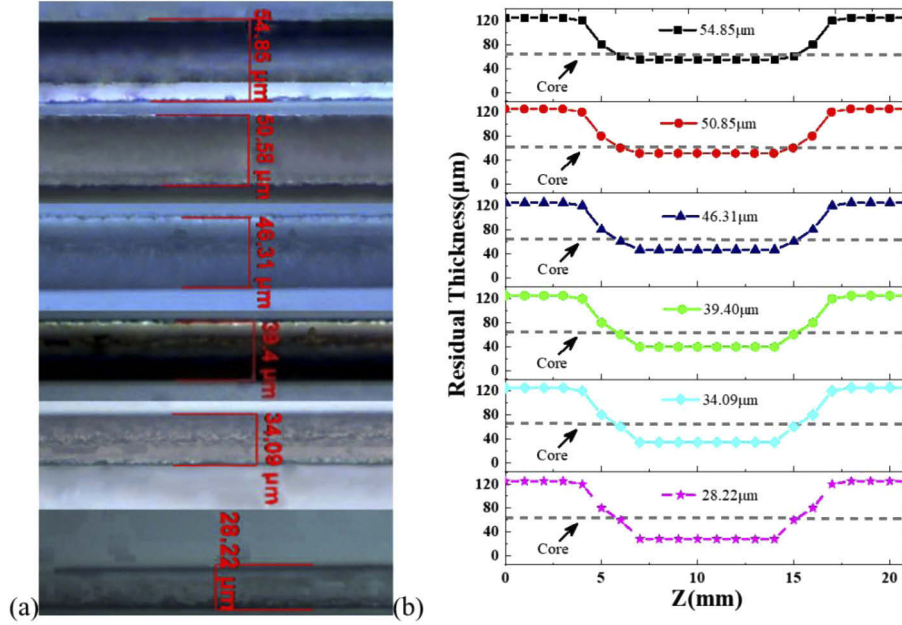
**Fig. 1.** (a) Transverse plane of conventional D-shaped fiber; (b) transverse plane of RT-enhanced D-shaped SMF; (c) isometric view of RT-enhanced D-shaped SMF; (d) front view of RT-enhanced D-shaped SMF.

Figure 2(a) shows the diagram of RT-enhanced D-shaped single mode fiber. Figure 2(b) is the cross section at the coreless flat section of CD-SMF observed by scanning electron microscope (SEM). As shown in the picture, the cross section of CD-SMF was D-shaped with a residual thickness of  $\sim 45 \mu\text{m}$ , indicating that the core of the SMF was removed. Figure 2(c) is a picture of the coreless flat section taken by the microscope (Zeiss, Axio Scope A1) with a  $20\times$  objective lens and a  $0.63\times$  eye lens. Figure 2(d) is a  $1\times 1 \mu\text{m}$  image with a data resolution of  $5\text{k} \times 5\text{k}$  points obtained by the atomic force microscope (Bioscope Catylyst Nanoscope V). It is indicated that the surface of the flat section of RT-enhanced D-shaped SMF fabricated by our custom fiber-polishing system was smooth.



**Fig. 2.** (a) Diagram of RT-enhanced D-shaped SMF, (b) cross section at the coreless flat section of CD-SMF observed by scanning electron microscope (SEM), (c) coreless flat section of CD-SMF observed by a microscope, (d) coreless flat section of CD-SMF observed by atomic force microscope (AFM).

Since the sensitivity of the RT-enhanced D-shaped SMF is closely related to the residual thickness, six single mode fibers with different RTs from 54.85  $\mu\text{m}$  to 28.22  $\mu\text{m}$  were fabricated by our custom fiber-polishing system. Figure 3(a) shows the pictures of D-shaped areas obtained with a microscope with a 20 $\times$  objective lens. Figure 3(b) showed the parameters of the six RT-enhanced D-shaped SMFs.



**Fig. 3.** (a) Microscopic image of the flat section of the RT-enhanced D-shaped SMFs. The RTs were measured as 54.85  $\mu\text{m}$ , 50.85  $\mu\text{m}$ , 46.31  $\mu\text{m}$ , 39.40  $\mu\text{m}$ , 34.09  $\mu\text{m}$ , and 28.22  $\mu\text{m}$ , respectively. (b) Variations of residual thicknesses for the six fabricated RT-enhanced D-shaped SMFs.

## 2.2. Analysis of multimode interference (MMI)

The light transmission path in the RT-enhanced D-shaped SMF is shown in the Fig. 4. The high orders in the fiber was induced by the multi reflections with angles of incidence on the curved surface in the transitional section 1. The efficiency of the MMI in the RT-enhanced D-shaped SMF was closely related to the RT. The RT-enhanced D-shaped SMF with different RTs led to different angles of incidence  $\theta$ . The input optical field of the coreless flat section of the RT-enhanced D-shaped SMF can be written as:

$$E_{in}(\gamma, \theta) = \sum_{m=1}^M \sum_{n=1}^N b_{m,n} \Psi_{m,n}(\gamma, \theta) \quad (1)$$

where  $\Psi_{m,n}(\gamma, \theta)$  was the guided mode of  $TE_{m,n}$  or  $TM_{m,n}$  in the coreless flat section. The subscripts  $m$  and  $n$  denote the node numbers of specific guided mode, where the mode field distribution varied with the azimuthal angle and along the radial direction respectively. The exciting  $b_{m,n}$  coefficient for the  $\Psi_{m,n}(\gamma, \theta)$  mode. The evolution of optical field along the coreless flat section was determined by the interference between the excited high-order modes:

$$E(\gamma, \theta, z) = \sum_{n=1}^N b_{0,n} \Psi_{0,n}(\gamma, \theta) \exp(j\beta_{0,n}z) \quad (2)$$

where  $\beta_{0,n}$  was the propagation constant of  $TM_{0,n}$  and  $TE_{0,n}$  modes.

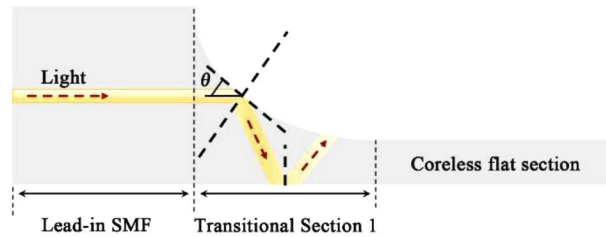


**Fig. 4.** Schematic of estimating the tilted angle  $\theta$  (slope  $t = \tan \theta$ ) of polished surface to excite the highest order mode in the cladding of RT-enhanced D-shaped SMF using an optical ray approximation.

### 3. Experiment

Figure 5 schematically illustrated the experimental setup used to evaluate the performance of the RI sensor based on RT-enhanced D-shaped SMFs. In order to make sure that coreless flat section of the fiber is fully in contact with the certified RI liquid (CRIL), the RT-enhanced D-shaped SMFs were positioned in a glass groove. The lead-in SMF and lead-out SMF were fixed on the glass substrate using ultra-violet glue. The lead-in SMF of the fiber was connected to a supercontinuum light source (SCS YSLSC-5-CFS). The lead-out SMF of the fiber was connected to the spectrometer optical spectrum analyzer (OSA YOKOGAW AQ6370D) with a resolution of 20 pm. The supercontinuum light source can provide light in the wavelength range of 450 nm-2400 nm with a peak power of 9 dBm at 1064 nm. The refractive index matching liquids (Cargille Labs) with a RI range from 1.430-1.444 were used as the standard samples to evaluate the sensor based on the RT-enhanced D-shaped SMF. Each time the refractive index matching liquids with the volume of 10  $\mu\text{L}$  was added to the glass groove, the corresponding transmission spectrum of RT-enhanced D-shaped SMF was recorded. Then the RT-enhanced D-shaped SMF was cleaned with 99.99% alcohol (Aldrich) before next test. The experiment was carried out in a fume hood.

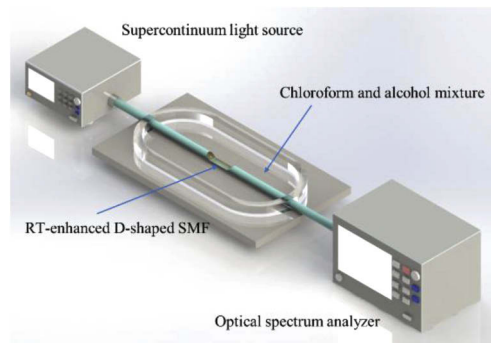


**Fig. 5.** Schematic diagram of experimental setup to evaluate the performance of the sensor based on the RT-enhanced D-shaped SMF.

### 4. Results and discussions

#### 4.1. Sensor evaluation of RI sensor based on RT-enhanced D-shaped SMF

The RI sensing performance of the fabricated RT-enhanced D-shaped SMFs with five different RTs were evaluated theoretically and experimentally. Since the D-shaped fiber with RT of 28.22  $\mu\text{m}$  shows a power of < 70 dB, the transmission spectrum was covered by the noise. This may be

the caused by the great insert loss resulted from such a small fiber residual thickness. Figures 6(a), 6(c), 6(e), 6(g) and 6(i), corresponding to RT-enhanced D-shaped SMF with the RT of 54.85  $\mu\text{m}$ , 50.85  $\mu\text{m}$ , 46.31  $\mu\text{m}$ , 39.4  $\mu\text{m}$  and 34.09  $\mu\text{m}$ , showed transmission spectra with a RI range of 1.430~1.444. Since the residual thickness has a significant influence on the mode interference in the fiber, as a result the dip wavelength shows a shift over a large range. In order to short the sensor response time, the authors measured only the effective wavelength ranges spanning the dip. Figures 6(b), 6(d), 6(f), 6(h) and 6(j) showed the simulated transmission light field along the optical fiber with RT of 54.85  $\mu\text{m}$ , 50.85  $\mu\text{m}$ , 46.31  $\mu\text{m}$ , 39.40  $\mu\text{m}$  and 34.09  $\mu\text{m}$ , respectively. It can be seen from the subgraphs the MMI efficiency of RT = 34.09  $\mu\text{m}$  is denser than others. A beam propagation module (Rsoft Inc.) was employed to simulate the transmission spectra and field evolution of the RT-enhanced D-shaped SMF. The geometrical parameters are: length of the flat section  $L_f = 8$  mm, lengths of the two transitional sections  $L_{t1} = L_{t2} = 4$  mm; the core RI = 1.4681 and a cladding RI = 1.4628. The core diameter was 8.2  $\mu\text{m}$  and the cladding diameter was 125  $\mu\text{m}$ . Here, the RTs in the simulations were set the same to analyze the RT-enhanced D-shaped SMF with different MMI efficiency. The curved polished surfaces of the transitional section 1 and 2 were modeled by a surface of an elliptic cylinder with a major axis of  $L_{t1}$  and a minor axis of  $(125 - \text{RT})$   $\mu\text{m}$ . With increasing of the RI, the wavelength dip shifted to longer wavelengths with an increasing slope.

According to the characteristic dips indicated by the arrows in Fig. 6, we could observe the shift of the dips and obtained the dependencies of the dip wavelength on the surrounding RI. Figure 7(a) shows the dip wavelength as a function of the surround refractive index from 1.305 to 1.444 obtained experimentally. The dip wavelength increased exponentially with the surrounding refractive index. In the RI range of 1.430~1.444 where the RI is close to the fiber core, the slope of the curve changed dramatically. The RI is high as the fiber core induced a strong evanescent wave on the fiber polishing surface, resulting in the interaction between the coreless flat section and surrounding refractive index matching liquid. As shown in Fig. 7(b), we calculated the sensitivity of sensor for different RTs in different RI ranges. With respect to the RT of 34.09  $\mu\text{m}$ , the sensor sensitivity in the RI range of 1.305-1.402 reached 487 nm/RIU which is 2.8 times larger than that of the 54.85  $\mu\text{m}$ . In the range of 1.430-1.444, the sensor sensitivity reached up to 10243 nm/RIU. Such a sensitivity can be attributed to the high multimode interference efficiency of the RT-enhanced effect in a D-shaped fiber.

#### 4.2. VOC evaporation monitoring

Chloroform ( $\text{CHCl}_3$ ) and alcohol ( $\text{C}_2\text{H}_5\text{OH}$ ) are important organic compounds in organic industrial chemistry and biology [31]. A short duration exposure of 50 ppm of chloroform can cause damage to human health. In this section, the residual thickness enhanced fiber sensor was developed for chloroform and alcohol mixture evaporation monitoring. Photodecomposition of chloroform occurs with light wavelength from 260 nm to near-UV ( $\sim 345$  nm) [32]. The experiment was carried in the dark room with negative pressure. The RI of a 99% chloroform and 1% alcohol mixture is measured to be  $\sim 1.44$  at room temperature [33]. Considering the ultrahigh sensitivity of sensor in the RI range of 1.430-1.444, the sensor system was developed for chloroform liquid monitoring based on a RT-enhanced D-shaped SMF with a RT of 34.09  $\mu\text{m}$ . The diagram of the sensor system was schematically shown in Fig. 5. The RT-enhanced D-shaped SMF was fixed on a glass substrate and embedded in the chloroform and alcohol mixture. The optical spectrum analyzer was used to record the spectra to trace the dip wavelength monitoring in real time. The spectrum spanning from 1250 nm to 1600 nm with the points of 1750 was record every 1 min.

Figure 8(a) is the variation of transmission spectra during the whole evaporation process of chloroform. The dip wavelength of the sensor showed a sharp redshift to  $> 1550$  nm in 30 mins and then a gradual blueshift to  $\sim 1450$  nm in 2 hours. Figure 8(b) depicts the variation of the

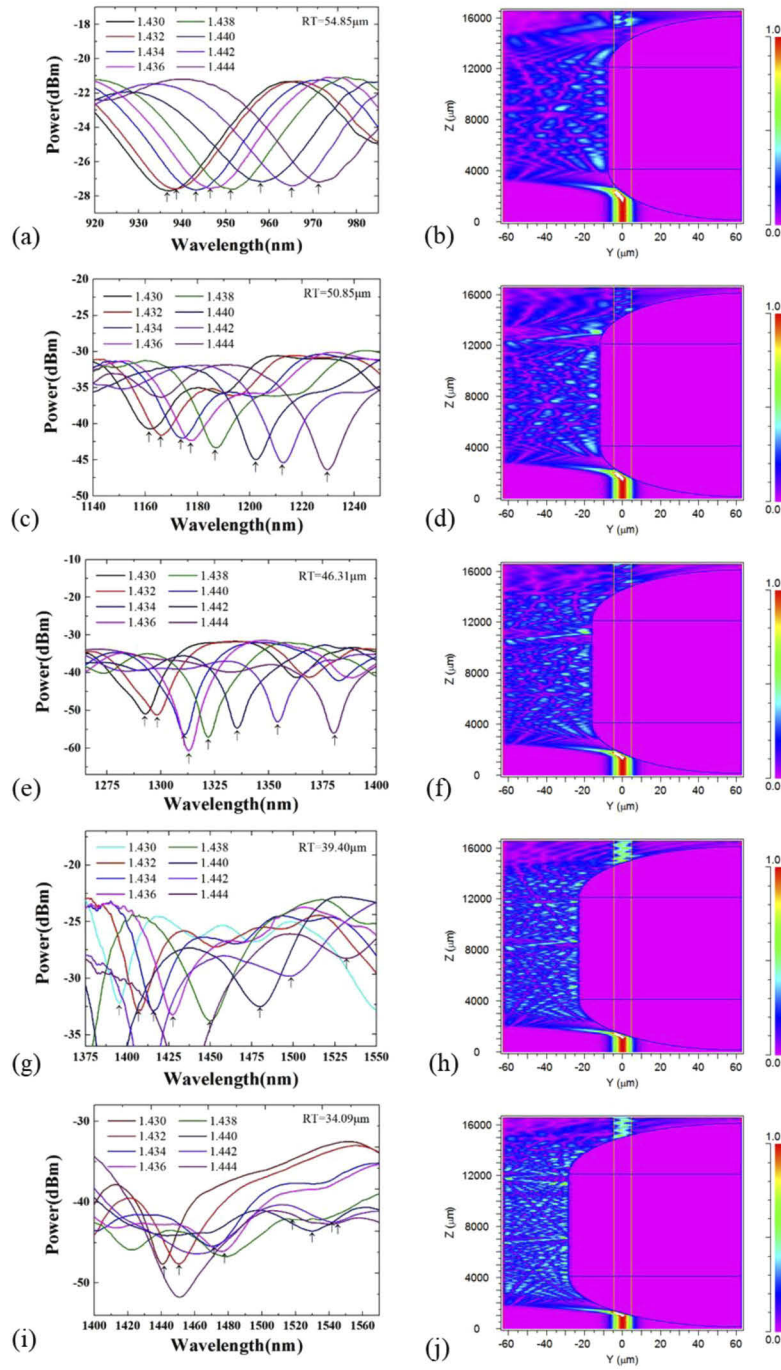


**Fig. 6.** The measured transmission spectra of the RT-enhanced D-shaped SMFs with RTs of (a) 54.85  $\mu\text{m}$ , (c) 50.85  $\mu\text{m}$ , (e) 46.3  $\mu\text{m}$ , (g) 39.40  $\mu\text{m}$  and (i) 34.09  $\mu\text{m}$ , respectively. Transmission of the light field along the optical fiber of (b) 54.85  $\mu\text{m}$ , (d) 50.85  $\mu\text{m}$ , (f) 46.31  $\mu\text{m}$ , (h) 39.4  $\mu\text{m}$  and (j) 34.09  $\mu\text{m}$ , respectively.

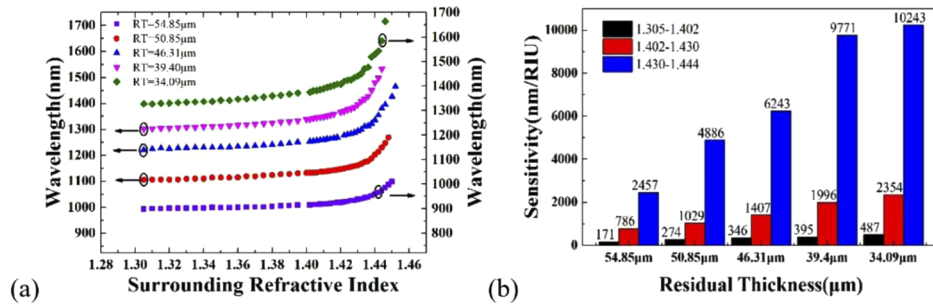


**Fig. 7.** (a) The dip wavelength of transmission spectra as the function of surrounding refractive index; (b) the calculated sensor sensitivities in three RI ranges.

shift of sensor transmission spectra. As a comparison, the transmission spectra of the sensor without chloroform was recorded at  $T = 0$  min.  $\Delta\lambda$  was defined as the shift of dip wavelength. According to the evaporation process of the liquid mixture, Fig. 8(b) was divided into four zones. Zone A and D represent the immersing and separating process of the fiber in liquid chloroform, respectively. Compared to the fiber sensor exposed to air, the immersion of chloroform resulted in a wavelength redshift of  $\sim 175$  nm. In Zone B, starting from 6 min to 27 min, the dip wavelength shifted to a longer wavelength with a  $\Delta\lambda$  of 267.6 nm. In a period of 128 minutes, the chloroform completely separated with the fiber sensor.

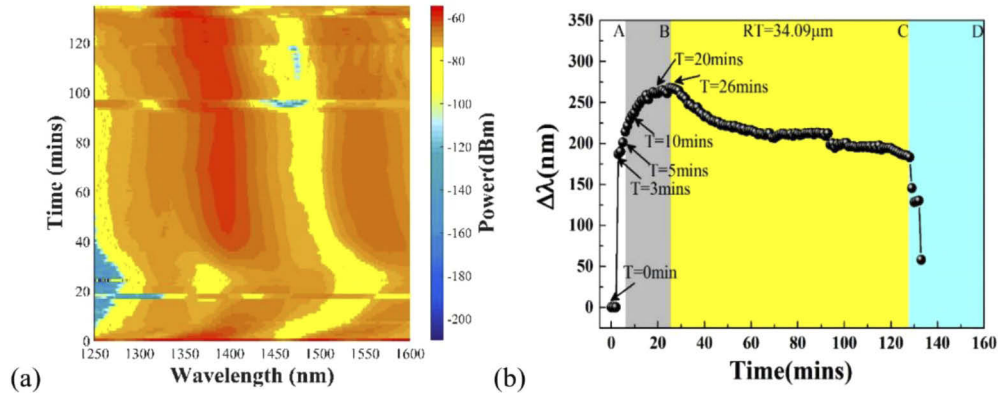


**Fig. 8.** On-line monitoring of the evaporation of chloroform and alcohol mixture.

The explanation of the phenomenon can be explained by the change of effective refractive index in the MMI. The schematic of Zone B of Fig. 8(b) can be described by Fig. 9(a), in which the fiber core was completely immersed in the mixture. The effective refractive index  $n_{\text{eff}}$  of external media can be expressed as:

$$n_{\text{eff}} = f(n_1, n_2) \quad (3)$$

where  $n_1$  and  $n_2$  are the refractive index of chloroform and alcohol respectively. Considering that the refractive index of alcohol and chloroform are  $\sim 1.36$  and  $\sim 1.44$  respectively, in this case the evaporation of alcohol resulted in an increasing  $n_{\text{eff}}$  in Zone B. Around the dividing line between Zone B and Zone C the wavelength shift  $\Delta\lambda$  becomes horizontal gradually. The schematic of Zone C of Fig. 8(b) can be described by Fig. 9(b), in which the fiber core was partly exposed to the air. With the evaporation of chloroform, the air started to dominate, and the effective

refractive index decreased gradually:

$$n_{eff} = f(n_1, n_3) \quad (4)$$

where  $n_3$  is the refractive index of air. Since the dip wavelength increased as the surrounding refractive index, the dip wavelength shows a red-shift in Zone B and a blue-shift in Zone C. The small deviation between the beginning and the ending of the dip wavelength was attributed to the impurity of the liquid mixture attached to the fiber.

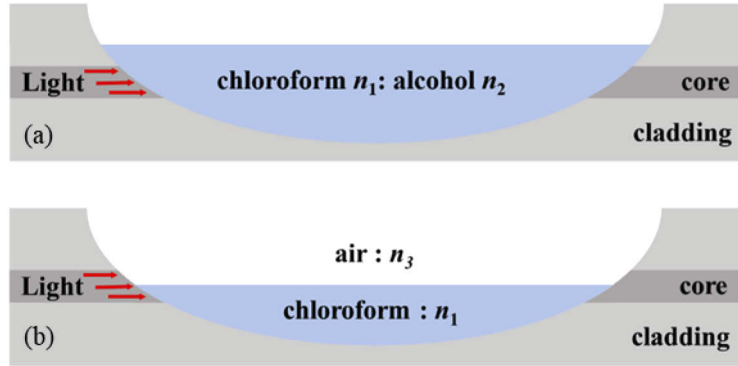


**Fig. 9.** The schematic diagram of Zone B (a) and Zone C (b).

## 5. Conclusions

An RT-enhanced D-shaped structure was manufactured on a single mode fiber for high sensitivity index sensing by means of custom-made ultra-precise side polishing system. Compared to other D-shaped fiber sensor, the developed D-shaped structure was on a communication single mode fiber with a cladding diameter of  $\sim 125 \mu\text{m}$  and a core diameter of  $\sim 9 \mu\text{m}$ . Ultra-precise wheel machining was used to polish the cladding and core of the single mode fiber. The absence of the fiber core leads to multi-reflection induced multi-modes interference in the D-shaped fiber wave guide. In this manuscript, the residual thickness (RT) enhancement effect in D-shaped fiber was investigated in detail. The RT enhancement was firstly quantified from  $54.85 \mu\text{m}$  to  $28.22 \mu\text{m}$ . It was found that the residual thickness of the RT-enhanced D-shaped SMF showed a significant impact on the transmission spectra and optical power loss of the fiber. Therefore, six different residual thicknesses from  $\sim 55 \mu\text{m}$  to  $\sim 28 \mu\text{m}$  were fabricated on different D-shaped SMF to evaluate the sensor performance. The transmission spectra of the six RT-enhanced D-shaped SMFs were investigate both theoretically and experimentally. Considering a compromise between the MMI efficiency and optical power loss, the optimum RT was determined to be  $\sim 34 \mu\text{m}$ . Benefiting from the RT-enhancement, the extinction ratio of  $\sim 15 \text{ dB}$  and the sensor sensitivity of  $10243 \text{ nm/RIU}$  in the range of  $1.43\text{-}1.44$  was achieved, corresponding to a refractive index resolution of  $1.9 \times 10^{-6} \text{ RIU}$ . Based on the RT-enhanced D-shaped fiber, a high-performance all-fiber sensor was developed for VOCs mixture evaporation monitoring. As proof of concept, the RT-enhanced D-shaped fiber sensor showed  $>2$  hours continuous on-line monitoring of the evaporation of chloroform and an alcohol mixture. The evaporation of alcohol and chloroform can be clearly distinguished in the monitoring process. The high sensitivity and fast response indicate that the RT-enhanced D-shaped fiber has a great potential in the real time monitoring in analytical chemistry and industrial applications. Compared to the index sensor based on gold-coated D-shaped photonic crystal fiber with a higher sensitivity of  $21700 \text{ nm/RIU}$  [34], the advantage of RT-enhanced D-shaped SMF is the easier fabrication, more cost-effective price and

better compatibility with the communication fiber systems. The using of single mode silica fiber will benefit the long-distance and large-scale distribution measurement. The sensor performance can be further improved by surface plasmon resonance by depositing specific materials on the D-shaped fiber surface [35].

## Funding

Aeronautical Science Foundation of China (201708W4001, 201808W4001); State Key Laboratory of Applied Optics (SKLAO-201914); Fundamental Research Funds for the Central Universities (21619402, 11618413); Foundation for Distinguished Young Talents in Higher Education of Guangdong (2018KQNCX009); Open foundation of CEPREI (NO. 19D09); Joint fund of pre-research for equipment, Ministry of Education of China (6141A02022124); Planned Science & Technology Project of Guangzhou (201707010396, 2016B010111003); Project of Guangzhou Industry Leading Talents (CXLJTD-201607); Key-Area Research and Development Program of Guangdong Province (2019B010138004, 2017A010102006, 2015B010125007); Natural Science Foundation of Guangdong Province (2016A030311019, 2016A030313079, 2017A030313375, 2019A1515011380, 2020B1515020024); National Natural Science Foundation of China (61601404, 61675092, 61705086); National Science Foundation (R3H685).

## Disclosures

The authors declare no conflicts of interest.

## References

1. B. Lee, "Review of the present status of optical fiber sensors," *Opt. Fiber Technol.* **9**(2), 57–79 (2003).
2. C. R. Biazoli, S. Silva, M. A. R. Franco, O. Frazão, and C. M. B. Cordeiro, "Multimode interference tapered fiber refractive index sensors," *Appl. Opt.* **51**(24), 5941–5945 (2012).
3. C. Y. He, J. B. Fang, Y. N. Zhang, Y. Yang, J. H. Yu, J. Zhang, H. Y. Guan, W. T. Qiu, P. J. Wu, J. L. Dong, H. H. Lu, J. Y. Tang, W. G. Zhu, N. Arsad, Y. Xiao, and Z. Chen, "High performance all-fiber temperature sensor based on coreless side-polished fiber wrapped with polydimethylsiloxane," *Opt. Express* **26**(8), 9686–9699 (2018).
4. Y. Gong, T. Zhao, Y. J. Rao, and Y. Wu, "All-fiber curvature sensor based on multimode interference," *IEEE Photonics Technol. Lett.* **23**(11), 679–681 (2011).
5. Q. Wang and G. Farrell, "All-fiber multimode-interference-based refractometer sensor: proposal and design," *Opt. Lett.* **31**(3), 317–319 (2006).
6. P. F. Wang, G. Brambilla, M. Ding, Y. Semenova, Q. Wu, and G. Farrell, "High-sensitivity, evanescent field refractometric sensor based on a tapered, multimode fiber interference," *Opt. Lett.* **36**(12), 2233–2235 (2011).
7. Y. Liu and L. Wei, "Low-cost high-sensitivity strain and temperature sensing using graded-index multimode fibers," *Appl. Opt.* **46**(13), 2516–2519 (2007).
8. S. Silva, O. Frazão, J. L. Santos, and F. X. Malata, "A reflective optical fiber refractometer based on multimode interference," *Sens. Actuators, B* **161**(1), 88–92 (2012).
9. L. V. Nguyen, D. Hwang, S. Moon, D. S. Moon, and Y. Chung, "High temperature fiber sensor with high sensitivity based on core diameter mismatch," *Opt. Express* **16**(15), 11369–11375 (2008).
10. J. E. Antonio-Lopez, J. J. Sanchez-Mondragon, P. LiKamWa, and D. A. May-Arrioja, "Fiber-optic sensor for liquid level measurement," *Opt. Lett.* **36**(17), 3425–3427 (2011).
11. M. Bachmann, P. A. Besse, and H. Melchior, "General self-imaging properties in  $N \times N$  multimode interference couplers including phase relations," *Appl. Opt.* **33**(18), 3905–3911 (1994).
12. H. N. Xu and Y. C. Shi, "Dual-mode waveguide crossing utilizing taper-assisted multimode-interference couplers," *Opt. Lett.* **41**(22), 5381–5384 (2016).
13. A. Maese-Novio, R. Halir, S. Romero-García, D. Pérez-Galacho, L. Zavargo-Peche, A. Ortega-Moñux, I. Molina-Fernández, J. G. Wangüemert-Pérez, and P. Cheben, "Wavelength independent multimode interference coupler," *Opt. Express* **21**(6), 7033–7040 (2013).
14. L. Zhang, J. M. Hu, J. H. Wang, and Y. Feng, "Tunable all-fiber dissipative-soliton laser with a multimode interference filter," *Opt. Lett.* **37**(18), 3828–3830 (2012).
15. N. Li, M. Y. Liu, X. J. Gao, L. Zhang, Z. X. Jia, Y. Feng, Y. Ohishi, G. S. Qin, and W. P. Qin, "All-fiber widely tunable mode-locked thulium-doped laser using a curvature multimode interference filter," *Laser Phys. Lett.* **13**(7), 075103 (2016).
16. Q. Q. Meng, X. Y. Dong, K. Ni, Y. Li, B. Xu, and Z. M. Chen, "Optical fiber laser salinity sensor based on multimode interference effect," *IEEE Sens. J.* **14**(6), 1813–1816 (2014).

17. H. Z. Dong, L. H. Chen, J. J. Zhou, J. H. Yu, H. Y. Guan, W. T. Qiu, J. L. Dong, H. H. Lu, J. Y. Tang, W. G. Zhu, Z. G. Cai, Y. Xiao, J. Zhang, and Z. Chen, "Coreless side-polished fiber: a novel fiber structure for multimode interference and highly sensitive refractive index sensors," *Opt. Express* **25**(5), 5352–5365 (2017).
18. Y. Li, Z. B. Liu, and S. S. Jian, "Multimode interference refractive index sensor based on coreless fiber," *Photonic Sens.* **4**(1), 21–27 (2014).
19. H. Fukano, T. Aiga, and S. Taue, "High-sensitivity fiber-optic refractive index sensor based on multimode interference using small-core single-mode fiber for biosensing," *Jpn. J. Appl. Phys.* **53**(4S), 04EL08 (2014).
20. S. M. Tseng and C. L. Chen, "Side-polished fibers," *Appl. Opt.* **31**(18), 3438–3447 (1992).
21. J. Y. Tang, J. J. Zhou, J. W. Guan, S. Long, J. H. Yu, H. Y. Guan, H. H. Lu, Y. H. Luo, J. Zhang, and Z. Chen, "Fabrication of side-polished single mode-multimode-single mode fiber and its characteristics of refractive index sensing," *IEEE J. Sel. Top. Quantum Electron.* **23**(2), 238–245 (2017).
22. C. H. Chen, T. C. Tsao, J. L. Tang, and W. T. Wu, "A multi-D-shaped optical fiber for refractive index sensing," *Sensors* **10**(5), 4794–4804 (2010).
23. L. Bilro, N. J. Alberto, L. M. Sá, J. D. L. Pinto, and R. Nogueira, "Analytical analysis of side-polished plastic optical fiber as curvature and refractive index sensor," *J. Lightwave Technol.* **29**(6), 864–870 (2011).
24. Y. H. Luo, Q. S. Wei, Y. Ma, H. H. Lu, J. H. Yu, J. T. Tang, J. B. Yu, J. B. Fang, J. Zhang, and Z. Chen, "Side-polished-fiber based optical coupler assisted with a fused nano silica film," *Appl. Opt.* **54**(7), 1598–1605 (2015).
25. Y. Xiao, J. Zhang, J. H. Yu, H. Z. Dong, Y. Y. Wei, Y. H. Luo, Y. C. Zhong, W. T. Qiu, J. L. Dong, H. H. Lu, H. Y. Guan, J. Y. Tang, W. G. Zhu, and Z. Chen, "Theoretical investigation of optical modulators based on graphene-coated side-polished fiber," *Opt. Express* **26**(11), 13759–13772 (2018).
26. V. K. S. Hsiao, Z. Li, Z. Chen, P. C. Peng, and J. Y. Tang, "Optically controllable side-polished fiber attenuator with photoresponsive liquid crystal overlay," *Opt. Express* **17**(22), 19988–19995 (2009).
27. S. C. Wen, C. W. Chang, C. M. Lin, H. A. Liu, V. K. S. Hsiao, J. H. Yu, and Z. Chen, "Light-induced switching of a chalcogenide-coated side-polished fiber device," *Opt. Commun.* **334**, 110–114 (2015).
28. Y. H. Luo, C. Y. Chen, K. Xia, S. H. Peng, H. Y. Guan, J. Y. Tang, H. H. Lu, J. H. Yu, J. Zhang, Y. Xiao, and Z. Chen, "Tungsten disulfide (WS<sub>2</sub>) based all-fiber-optic humidity sensor," *Opt. Express* **24**(8), 8956–8966 (2016).
29. Y. M. Huang, W. G. Zhu, Z. B. Li, G. L. Chen, L. H. Chen, J. J. Zhou, H. Lin, J. W. Guan, W. X. Fang, X. Liu, H. Z. Dong, J. Y. Tang, H. Y. Guan, H. H. Lu, Y. Xiao, J. Zhang, H. C. Wang, Z. Chen, and J. H. Yu, "High-performance fibre-optic humidity sensor based on a side-polished fibre wavelength selectively coupled with graphene oxide film," *Sens. Actuators, B* **255**, 57–69 (2018).
30. H. H. Lu, Z. W. Tian, H. P. Yu, B. Yang, G. Y. Jing, G. Z. Liao, J. Zhang, J. H. Yu, J. Y. Tang, Y. H. Luo, and Z. Chen, "Optical fiber with nanostructured cladding of TiO<sub>2</sub> nanoparticles self-assembled onto a side polished fiber and its temperature sensing," *Opt. Express* **22**(26), 32502–32508 (2014).
31. S. L. Rosenthal, "A review of the mutagenicity of chloroform," *Environ. Mol. Mutagen.* **10**(2), 211–226 (1987).
32. W. H. S. Yu and M. H. J. Wijnen, "Photolysis of Chloroform in the Presence of Ethane at 25°C," *J. Chem. Phys.* **52**(5), 2736–2739 (1970).
33. I. Z. M. Ahad, S. W. Harun, S. N. Gan, and S. W. Phang, "Polyaniline (PANI) optical sensor in chloroform detection," *Sens. Actuators, B* **261**, 97–105 (2018).
34. T. Wu, Y. Shao, Y. Wang, S. Cao, W. Cao, F. Zhang, C. Liao, J. He, Y. Huang, M. Hou, and Y. Wang, "Surface plasmon resonance biosensor based on gold-coated side-polished hexagonal structure photonic crystal fiber," *Opt. Express* **25**(17), 20313–20322 (2017).
35. S. Cao, Y. Shao, Y. Wang, T. Wu, L. Zhang, Y. Huang, F. Zhang, C. Liao, J. He, and Y. Wang, "Highly sensitive surface plasmon resonance biosensor based on a low-index polymer optical fiber," *Opt. Express* **26**(4), 3988–3994 (2018).